magnetochemistry

MDPI

Article

Adjusting the Magnetic Properties of ZrO_2:Mn Nanocrystals by Changing Hydrothermal Synthesis Conditions

Izabela Kuryliszyn-Kudelska [1,*], Witold Dobrowolski [1], Monika Arciszewska [1], Artur Małolepszy [2], Leszek Stobinski [2] and Roman Minikayev [1]

[1] Institute of Physics, Polish Academy of Sciences, Al. Lotników 32/46, 02-668 Warsaw, Poland; dobro@ifpan.edu.pl (W.D.); arcis@ifpan.edu.pl (M.A.); minik@ifpan.edu.pl (R.M.)

[2] Faculty of Chemical and Process Engineering, Warsaw University of Technology, Waryńskiego 1, 00-645 Warsaw, Poland; Artur.Malolepszy@pw.edu.pl (A.M.); Leszek.Stobinski@pw.edu.pl (L.S.)

* Correspondence: kuryl@ifpan.edu.pl; Tel.: +48-22-116-3299

Received: 27 April 2018; Accepted: 11 June 2018; Published: 13 June 2018

Abstract: The aim of the present work was to study the magnetic properties of ZrO_2(Mn) nanocrystals prepared by microwave-assisted hydrothermal synthesis using three different precursors: $KMnO_4$, $MnCl_2$, and $Mn(NO_3)_2$. The structural characterization was performed by means of X-ray diffraction. The morphology of the samples was studied by using STEM microscopy. The magnetic properties were studied by means of alternating current (AC) susceptibility (at a small AC magnetic field with amplitude not exceeding 5 Oe) and direct current (DC) magnetization (up to 9 T). All of the samples demonstrated Curie–Weiss behavior at higher temperatures with negative values of the Curie–Weiss temperature θ. It was shown that the conditions of the synthesis, e.g., pH and the type of precursor, can be adjusted to decrease the value of the Curie–Weiss temperature and reduce antiferromagnetic interactions.

Keywords: nanostructured materials; oxide materials; zirconium dioxide; magnetic measurements

1. Introduction

Zirconia (ZrO_2) has attracted great interest for its unique physical properties and potential applications in electronics and optoelectronics. Zirconia is an important material used in industry in solid fuel cells, catalytic agents, ceramics, and gas sensors [1–4]. ZrO_2 is a *p*-type semiconductor with a large and indirect band gap (6.1 eV in the cubic ground state phase, 5.87 and 5.83 eV in the tetragonal and monoclinic ones, respectively) [5]. Pure zirconia has a monoclinic structure at room temperature. It exhibits structural transformations when the temperature increases: first transforming to tetragonal form at approximately 1170 °C and then to a cubic fluorite structure at around 2370 °C [6]. Thus, depending on the synthesis method and thermal treatment, monoclinic, tetragonal, cubic, or a mixture of these phases might be present in zirconia-based crystals. In view of their applications, the cubic and tetragonal phases are important. The two high-temperature phases (cubic and tetragonal) have excellent mechanical, thermal, and dielectric properties, which make ZrO_2 an ideal candidate for protective coatings, high-k dielectric materials, and chemically inert refractory materials [7]. The room temperature stabilization of these polymorphs is commonly achieved by the addition of another cation, such as Ca^{2+}, Y^{3+}, Ce^{4+}, Ga^{3+}, or Mg^{2+} [7–10]. It was shown that Mn^{2+} cations stabilize either the tetragonal or cubic form at increasing content [11–14].

In the context of commercial applications, doped magnetic oxides are of particular interest. As a typical semiconducting host, metal oxides, such as ZnO, TiO_2, SnO_2, or Cu_2O, are usually

considered [15–17]. In particular, many interesting reports exist in the area of transition metal (TM)-doped nanosized zirconia (ZrO_2); (see, e.g., [14,18]) and references therein. In many cases, it was shown that TM doping does not play a crucial role and defects vacancies are responsible for the observed magnetism [19,20]. It was theoretically predicted by the use of ab initio electronic structure calculations that cubic Mn-stabilized ZrO_2 should be ferromagnetic above 500 K [21]. Boujnah et al. calculated using the density functional theory (DFT) with the generalized gradient approximation (GGA) and the modified Becke–Johnson (mBJ) approach that a ferromagnetically ordered configuration is the ground state in Mn-doped cubic ZrO_2 [22].

There are several experimental studies on ZrO_2 doped with Mn. However, the magnetic properties of Mn-doped ZrO_2 are not fully understood. The solubility of TM ions in ZrO_2 host material is fairly low and the magnetic cluster formation is very often responsible for the observed magnetic properties [14,23,24]. No evidence of long-range ferromagnetic ordering was reported in nanoparticles of ZrO_2 doped with Mn prepared either by the coprecipitation method [23] or by the nonaqueous sol-gel approach in benzyl alcohol [14]. Yu et al. found the presence of Mn_2O_3 secondary phase for nanosized samples with Mn content above $x = 0.25$ [23]. They observed paramagnetic behavior for samples below this Mn content. Pucci et al. observed two types of magnetic behavior: paramagnetic behavior for pristine nanocrystals and ferromagnetic behavior due to the presence of Mn_3O_4 phase after calcination [14]. Clavel et al. reported paramagnetic behavior for nanosized ZrO_2:Mn samples prepared by the benzyl alcohol route [24]. Paramagnetic behavior was reported for polycrystalline Y-stabilized tetragonal zirconia with up to 10% of Mn prepared by the solid state method by equilibrium [25]. For samples doped with higher Mn content (15% and 20% of Mn), local ferrimagnetic ordering was observed due to the Mn_3O_4 secondary phase. Zippel et al. observed defect-induced room temperature ferromagnetism (RTFM) for both undoped and Mn-doped ZrO_2 films grown by pulsed-laser deposition [26]. For cubic ZrO_2:Mn film, a noticeable ferromagnetic saturation magnetization at 5 K was observed. The authors correlated the observed ferromagnetism with a high density of dislocations. Hong et al. [27] found that cubic Mn-doped ZrO_2 films are ferromagnetic with T_C above 400 K. The observed ferromagnetism was mainly due to the ferromagnetic (FM) Mn–Mn interactions via oxygen intermediates. The authors revealed that differently from the cubic case, FM in monoclinic Mn-doped ZrO_2 films does not come only via exchange interactions, but also from defects. Kumar et al. synthesized nanostructures of tetragonal Mn-doped ZrO_2 and the observed room temperature ferromagnetism originated from the oxygen vacancies [28].

Despite a number of available reports and experimentally observed evidence for the ferromagnetism of magnetic oxides, there is still an open question about the origin of magnetism in these compounds. The aim of the present study is to examine the influence of the preparation conditions on the structural and magnetic properties of the resultant nanosized materials. In particular, from the point of view of future applications, we aim to stabilize high temperature ZrO_2 phases (tetragonal or cubic). We used a wet chemical microwave-assisted hydrothermal method to synthesize nanosized samples. The advantage of this technique is the really low temperature treatment, short processing time, use of simple equipment, and, additionally, the method is environmentally friendly. To the best of our knowledge, this method has not yet been used to synthesize ZrO_2 with Mn. In the previous paper, we studied the magnetic and structural properties of ZrO_2 doped with Fe [29]. We complete our experimental research about the effect of doping with TM on the magnetic properties of nanosized ZrO_2.

2. Sample Preparation and Experimental Methods

The nanocrystalline samples of ZrO_2 doped with Mn were obtained by using the microwave-assisted hydrothermal method (Magnum II microwave reactor, ERTEC, Wroclaw, Poland). Two series of the samples were prepared. In the first series, the appropriate amounts of $ZrOCl_2 \cdot 8H_2O$ (puriss. p.a. $\geq$99.5%, Merck, Saint Louis, MO, USA) and $KMnO_4$ (puriss p.a. $\geq$99.5%, Chempur, Piekary Slaskie, Poland) were dissolved in distilled water. Seventy-three milliliters (73 mL) of 0.05 M

$ZrOCl_2$ was used and 8 mL of $KMnO_4$ with different concentrations was added. An amount of 0.05 M $KMnO_4$ corresponded to 4.9 wt % Mn nominal concentration in the sample, and 0.2 M $KMnO_4$ corresponded to 19.5 wt % Mn nominal concentration in the sample. The obtained solution was put in an ultrasonic bath. The desired pH of the mixture (pH = 3, 7, 9) was adjusted by using 1 M NaOH (puriss p.a. ≥98.8%, Chempur, Piekary Slaskie, Poland). The microwave-assisted synthesis was conducted during 20 min in a reactor under a pressure of 55 bar. The reaction temperature was equal to 523 K. In the second series of the samples, we used two different precursors: $MnCl_2$ (puriss. p.a. ≥98.0%, Merck, Saint Louis, MO, USA) and $Mn(NO_3)_2$ (purum p.a. ≥97.0%, Merck, Saint Louis, MO, USA). In this case, we used 0.05 M $MnCl_2/Mn(NO_3)_2$, which corresponded to 4.9 wt % Mn nominal concentration in the sample, and 0.1 M $MnCl_2/Mn(NO_3)_2$, which corresponded to 9.8 wt % Mn nominal concentration in the sample. Seventy-three milliliters (73 mL) of 0.05 M $ZrOCl_2$ and 8 mL of $MnCl_2/Mn(NO_3)_2$ (with the two different concentrations given above) were used. The pH = 9 was adjusted in the second method of synthesis. The microwave assisted synthesis was conducted during 20 min in the reactor under a pressure of 55 bar. The reaction temperature was equal to 523 K. Two undoped reference samples were synthesized with 0.05 M $ZrOCl_2$ precursor for pH = 3 and pH = 7. The procedure of synthesis used allowed us to study the influence of various precursors as well as the pH of the mixture on structural and magnetic properties of the resultant samples. The details of the synthesis procedure are collected in Table 1.

The high resolution X-ray diffraction measurements were performed by using a Philips X'Pert Pro MPD Alpha1 Bragg–Brentano powder diffractometer (Cu K_α radiation was used, Malvern Panalytical, Eindhoven, the Netherlands). The morphology of the samples was studied by using a Hitachi s5500 scanning-transmission electron microscope (STEM, HITACHI, Tokyo, Japan). The magnetic properties were studied by using an AC/DC Lake Shore 7000 magnetometer (Lake Shore Cryotronics, Inc., Westerville, OH, USA). Alternating current (AC) magnetic susceptibility χ measurements in the temperature range 4.2–160 K were performed. The real, $Re(\chi)$, as well as the imaginary, $Im(\chi)$, parts of the magnetic susceptibility were collected in an AC magnetic field of frequency (f) range 7–10,000 Hz and amplitude not exceeding 5 Oe. Magnetization (M) was measured using the extraction technique in a magnetic field of up to 9 T.

3. Results and Discussion

3.1. XRD and STEM Characterization

STEM images for four representative samples for low (P5, P12) and high Mn concentration (P11, P6), prepared with pH = 9, are presented in Figure 1a–d. In the sample P5 with 4.9 wt % of Mn synthesized with the use of $KMnO_4$ precursor (Figure 1a), one can distinguish an agglomerated oval with a size between around 5 nm and 15 nm as well as cube nanograins with a size not exceeding 20 nm. For the P12 sample, prepared using $Mn(NO_3)_2$ precursor with 4.9 wt % of Mn, oval agglomerated nanocrystals are visible with a size between around 5 nm and 15 nm (Figure 1b). For the P11 ZrO_2 sample with 9.8 wt % of Mn prepared with the use of $Mn(NO_3)_2$ precursor, smaller (a size at around 5–7 nm) and agglomerated nanocrystals are visible. For this sample, only oval nanograins are observed (Figure 1c). The degree of agglomeration is lower than that in the P12 sample. The results for a higher content of Mn are presented in Figure 1d. The highest degree of agglomeration is observed for the P6 sample with higher doping, e.g., 19.5 wt % of Mn (Figure 1d). The sample was prepared by the use of $KMnO_4$ precursor. In this case, small oval nanograins (not exceeding 10 nm) and larger non-oval agglomerates (in size around 20 nm and above) are observed. In the samples prepared by use of $Mn(NO_3)_2$ precursor (P11 and P12), only oval nanograins are observed. For samples prepared with $KMnO_4$ precursor, oval and non-oval nanograins are visible.

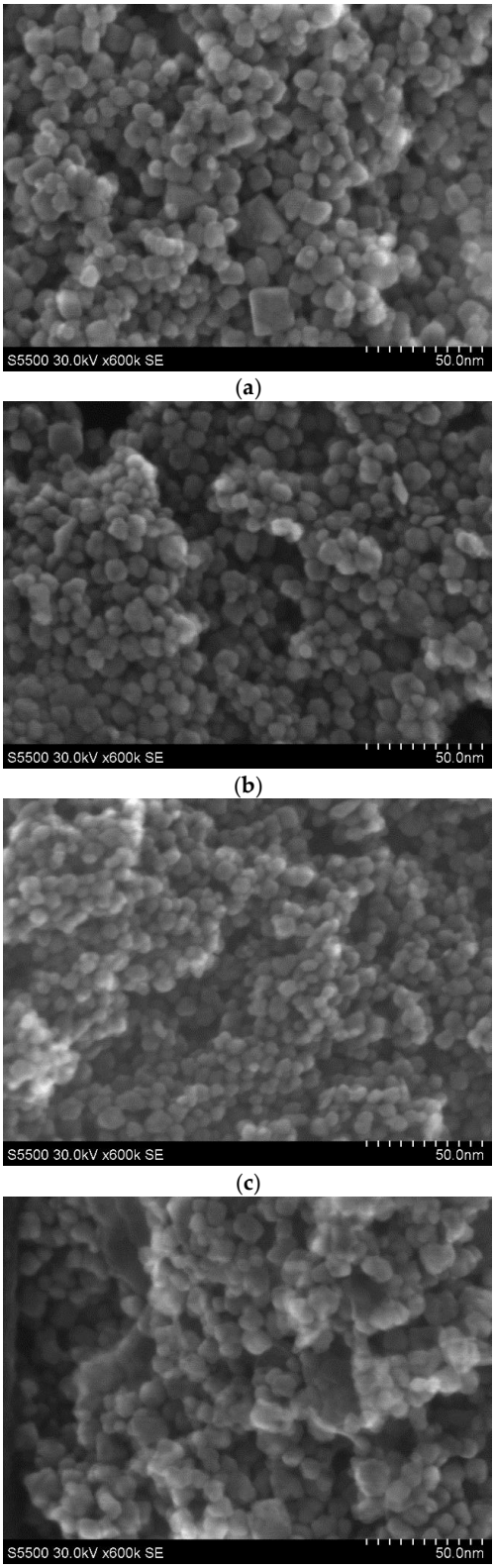

Figure 1. STEM images for samples of nanosized ZrO_2 doped with Mn: (**a**) the P5 sample doped with 4.9 wt % of Mn prepared with $KMnO_4$ precursor; (**b**) the P12 sample doped with 4.9 wt % of Mn prepared with $Mn(NO_3)_2$ precursor; (**c**) the P11 sample doped with 9.8 wt % of Mn prepared with the use of $Mn(NO_3)_2$ precursor; (**d**) the P6 sample doped with 19.5 wt % of Mn prepared with the use of $KMnO_4$ precursor.

X-ray diffraction patterns for all of the studied samples are shown in Figure 2a–e. For samples doped with 4.9 wt % of Mn and 9.8 wt % of Mn, no additional reflections due to the secondary phases are observed. The figures show broad diffraction peaks due to the nanometric size of zirconia crystals. Since the diffraction peaks are broad, the separation of monoclinic (m), tetragonal (t), and cubic (c) phases in nanosized ZrO_2 is a difficult task. The experimental strategy was based on the detection of a single, well-isolated peak belonging to one phase only. In Figure 2a, the results of measurements performed for samples with 4.9 wt % of Mn prepared with the use of $KMnO_4$ precursor for different pH values (P7 with pH = 3, P3 with pH = 7, P5 with pH = 9) are shown. Two ZrO_2 crystal phases, tetragonal and monoclinic, are detected. The well-isolated peak belonging to the monoclinic phase $m(-111)$ and the peak belonging to the tetragonal phase $t(102)$ are clearly visible. Figure 2b shows, as an example, the refinement results of the XRD pattern obtained for the sample P3. XRD data allowed us to determine a mean crystalline size, d, in the prepared samples by the use of Scherrer's formula [30]. The results of XRD analysis are gathered in Table 1. The tetragonal ZrO_2 crystal phase is dominant. The size of nanocrystals, determined from XRD, is smaller for the tetragonal crystal phase. For this crystal phase, nanocrystals with sizes of ~7 nm are observed. For monoclinic phase, larger values were determined, between ~10 nm and 17 nm.

For two samples doped with 4.9 wt % of Mn and prepared with $MnCl_2$ and $Mn(NO_3)_2$ precursors, cubic and monoclinic ZrO_2 crystal phases are observed. The results of XRD studies are shown in Figure 2c. For these two precursors, tetragonal ZrO_2 was not detected. The isolated peak belonging to the monoclinic phase $m(-111)$ is clearly visible. The results of the analysis are gathered in Table 1. For $MnCl_2$ and $Mn(NO_3)_2$ precursors, the amount of monoclinic ZrO_2 phase is much lower (only up to 6%) in comparison with the synthesis conducted with the $KMnO_4$ precursor. The cubic ZrO_2 crystal phase is dominant for the $MnCl_2$ and $Mn(NO_3)_2$ precursors. The size of nanocrystals for cubic crystal phase is equal to ~7 nm. The obtained data did not allow us to determine the size of crystallites for monoclinic phase.

Figure 2d shows XRD patterns and Rietveld refinement for samples doped with 9.8 wt % of Mn ($MnCl_2$ and $Mn(NO_3)_2$). In this case, we observed only cubic ZrO_2 crystal phase. The mean size of nanocrystals is at around 6 nm. STEM studies also revealed that smaller nanocrystallites for the P11 sample (9.8 wt % of Mn) are observed than for the P12 sample (4.9 wt % of Mn).

In the case of the $KMnO_4$ precursors, the samples were also doped with a higher Mn content: 19.5 wt % of Mn. The samples were prepared for three different pH values (pH = 3, 7, 9) as in the case of 4.9 wt % of Mn. Figure 2e shows the results of XRD measurements and Rietveld refinement for the P8 (pH = 3), P4 (pH = 7), and P6 (pH = 9) samples. Tetragonal ZrO_2 crystal phase and monoclinic ZrO_2 crystal phase are present. For sample P4 (pH = 7), an additional, undesirable NaCl structure was detectable. The formation of the small amount of this nonmagnetic phase can be a result of the conducted synthesis procedure with the used precursors. An additional undesired phase was also observed for sample P8 (pH = 3). However, the obtained XRD data did not allow us to identify it. Nevertheless, we excluded here the formation of manganese oxide phases. The analysis of the obtained data shows that in the case of the $KMnO_4$ precursor, the increase of Mn doping did not allow us to reduce the monoclinic ZrO_2 crystal phase. For the tetragonal crystal phase, nanocrystallites in the size of ~7–8 nm are observed; for the monoclinic crystal phase, the size of nanocrystallites is between 11 and 17 nm.

Figure 2f shows XRD patterns and Rietvield refinement for undoped ZrO_2 samples prepared with two different pH values, pH = 3 and pH = 7. In this case, monoclinic and cubic crystal phases were determined.

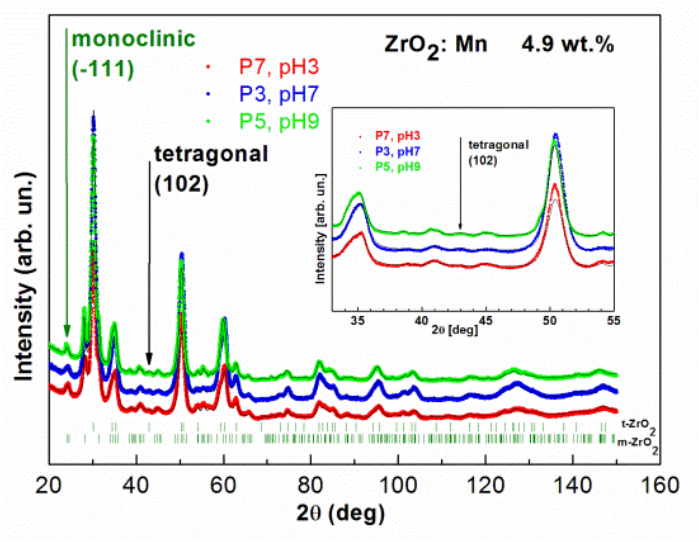

(**a**)

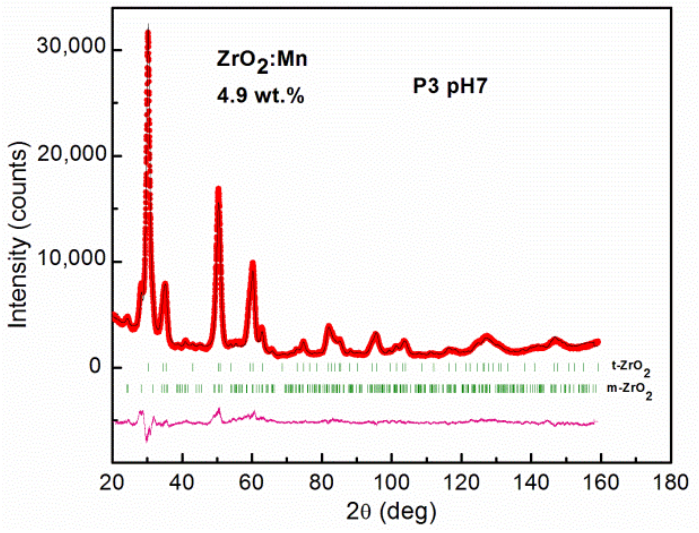

(**b**)

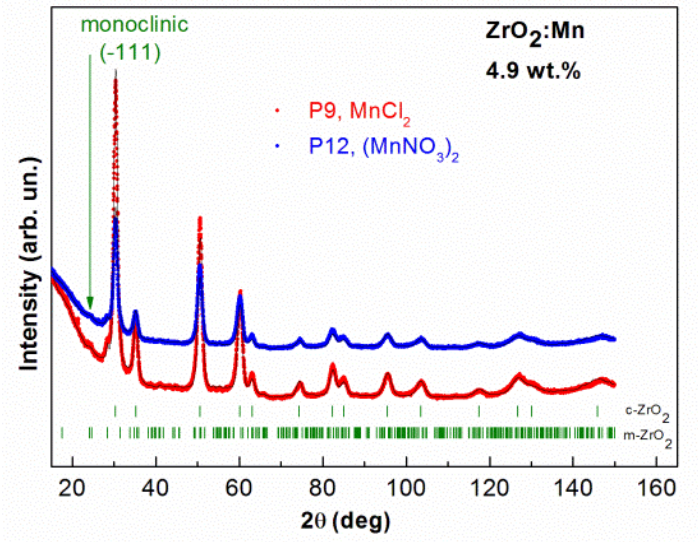

(**c**)

Figure 2. *Cont.*

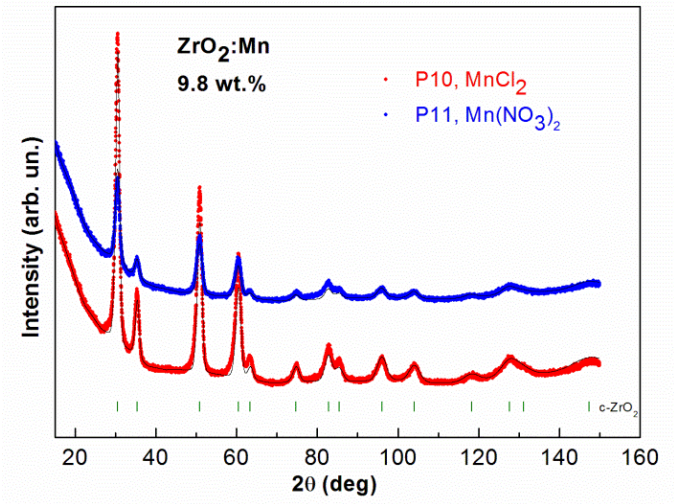

(**d**)

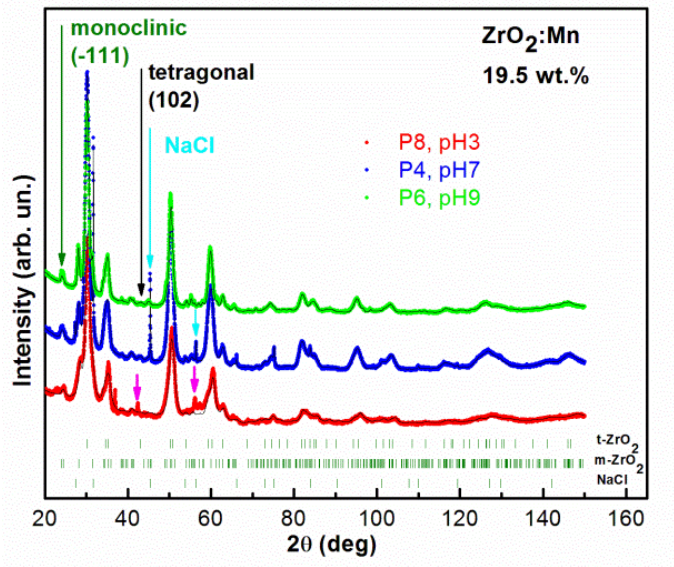

(**e**)

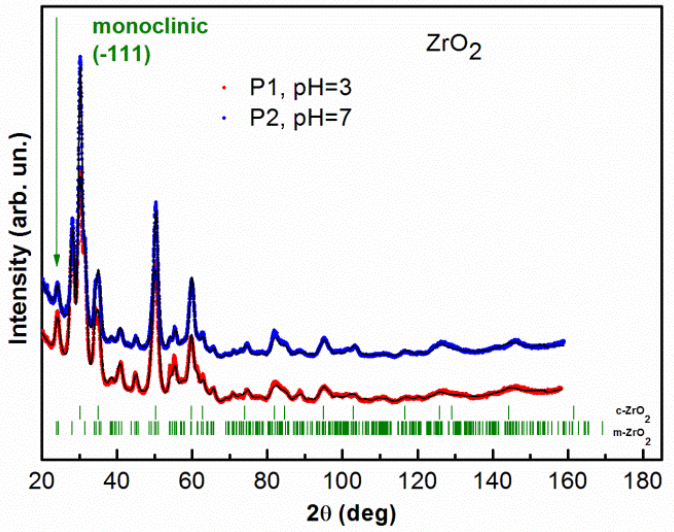

(**f**)

Figure 2. The observed XRD patterns (red, blue, and green lines) and Rietveld refinement (black line) of: (**a**) ZrO_2 doped with 4.9 wt % of Mn prepared by the use of $KMnO_4$ precursor with different pH values,

pH = 3, 7, 9; (**b**) ZrO_2 doped with 4.9 wt % of Mn prepared by the use of $KMnO_4$ precursor with pH = 7; the lowest curve (pink) is the difference between the observed and calculated XRD patterns; (**c**) ZrO_2 doped with 4.9 wt % of Mn prepared with $MnCl_2$ and $Mn(NO_3)_2$ precursors; (**d**) ZrO_2 doped with 9.8 wt % of Mn prepared with $MnCl_2$ and $Mn(NO_3)_2$ precursors; (**e**) ZrO_2 doped with 19.5 wt % of Mn prepared by the use of $KMnO_4$ precursor with different pH values, pH = 3, 7, 9; (**f**) ZrO_2 prepared with different pH values, pH = 3, 7. The vertical bars indicate the expected Bragg reflection positions. The isolated peaks attributed to the monoclinic ZrO_2 are marked with the green arrows. The isolated peaks attributed to the tetragonal ZrO_2 are marked with black arrows. The blue arrows indicate an additional NaCl crystal structure (P4 sample). The pink arrows indicate the observed additional unidentified phase for the P8 sample.

Table 1. The details of the synthesis and the results of XRD studies (the obtained percentage of determined crystal phases and the mean size of nanocrystallites *D*) for the undoped samples and the samples prepared with $KMnO_4$, $MnCl_2$, and $Mn(NO_3)_2$. The "+" means that the determined crystalline phase was detected; however, the experimental data did not allow us to determine the percentage of obtained crystal phases and/or the mean size of nanocrystallites *D*.

Sample Name and Precursor	Nominal Content of Mn pH	ZrO_2 (Cubic)		ZrO_2 (Tetragonal)		ZrO_2 (Monoclinic)		NaCl		Additional Phase	
		%	*D* (nm)	%	*D* (nm)	%	*D* (nm)	%	*D* (nm)	%	*D* (nm)
P7 $KMnO_4$	4.9 wt % pH 3	-	-	77.2	7	22.8	10.8	-	-	-	-
P3 $KMnO_4$	4.9 wt % pH 7	-	-	88.9	7.1	11.1	10.1	-	-	-	-
P5 $KMnO_4$	4.9 wt % pH 9	-	-	87.4	7.5	12.6	17	-	-	-	-
P8 $KMnO_4$	19.5 wt % pH 3	-	-	+	+	+	+	-	-	+	+
P4 $KMnO_4$	19.5 wt % pH 7	-	-	73.5	7.3	15.1	10.8	11.4	+	-	-
P6 $KMnO_4$	19.5 wt % pH 9	-	-	84.8	8.1	15.2	17	-	-	-	-
P9 $MnCl_2$	4.9 wt % pH 9	95.4	7.1	-	-	4.6	+	-	-	-	-
P12 $Mn(NO_3)_2$	4.9 wt % pH 9	94.2	6.7	-	-	5.8	+	-	-	-	-
P10 $MnCl_2$	9.8 wt % pH 9	100	6.6	-	-	-	-	-	-	-	-
P11 $Mn(NO_3)_2$	9.8 wt % pH 9	100	5.8	-	-	-	-	-	-	-	-
P1 $ZrOCl_2$	- pH 3	50	5	-	-	50	7.3	-	-	-	-
P2 $ZrOCl_2$	- pH 7	64	6.1	-	-	36	8.2	-	-	-	-

It was already reported that Mn doping leads to the stabilization of tetragonal and cubic phases of ZrO_2. We demonstrated that the formation of high-temperature crystal phases strongly depends on the synthesis conditions, e.g., the type of the precursor. Our results showed that using $KMnO_4$ precursor leads to the formation of tetragonal crystal phase. It should be noticed that the assignment of cubic and tetragonal zirconia structures, based only on the X-ray diffraction analysis, can be misleading because these two structures are very similar. The analysis of the experimental patterns is also complicated in this case due to the intrinsic broadening of ZrO_2 peaks. Nevertheless, our experimental results suggest

that using KMnO4 precursor does not lead to the formation of cubic phase of ZrO_2. We observed that, for $KMnO_4$ precursor, the increase of the nominal concentration of Mn (from 4.9 wt % of Mn to 19.5 wt % of Mn) does not lead to a decrease in the amount of monoclinic phase and an increase of tetragonal phase. However, we noticed that the increase of pH values decreases the amount of the monoclinic phase and increases the amount of the tetragonal phase. For example, in the case of a nominal concentration of Mn equal to 4.9 wt %, the increase of pH from 3 to 9 leads to an increase in the amount of the tetragonal form from 77.2% to 87.4%. Using $MnCl_2$ and $Mn(NO_3)_2$ allows us to obtain the cubic phase of ZrO_2. For a nominal concentration of Mn equal to 9.8 wt %, we obtained pure cubic ZrO_2 phase. For a sample with a lower nominal concentration of Mn, equal to 4.9 wt %, and pH = 9, we obtained 12.6% of monoclinic phase for the $KMnO_4$ precursor, 4.6% for the $MnCl_2$ precursor, and 5.8% for the $Mn(NO_3)_2$ precursor. In the case of the $MnCl_2$ and $Mn(NO_3)_2$ precursors, we observed a much lower amount of monoclinic phase in comparison to the synthesis with the $KMnO_4$ precursor.

3.2. Magnetic Studies

Figure 3a–d show the results of the AC magnetic susceptibility measurements. The inverse magnetic susceptibility and the susceptibility for selected samples are plotted as functions of temperature. The imaginary part of the AC magnetic susceptibility is close to zero and the temperature is independent for all of the measured samples.

For all of the investigated samples, the high-temperature behavior of the inverse low-field susceptibility χ^{-1} was nearly linear. All of the ZrO_2:Mn samples exhibited Curie–Weiss law behavior at high temperatures. We did not observe the presence of features that could be related to the secondary magnetic phases. In particular, for sample P8, where unidentified additional phase was detected by XRD measurements, only Curie–Weiss behavior is observed. The diamagnetic host lattice temperature dependence was measured for pure nanocrystalline ZrO_2 (P1 and P2 samples: $\chi_{\mathrm{dia}} = -0.6 \times 10^{-6}$ emu/g) and was subtracted from the measured magnetic susceptibility. The experimental methods for the magnetic materials are described (e.g., in [31,32]).

At higher temperatures, the AC mass susceptibility can be described by the formula [32]:

$$\chi = C(x)/(T - \theta(x)), \quad (1)$$

where $C(x) = C_0 x$ and $\theta(x)$ is the Curie–Weiss temperature. C_0 is defined as: $C_0 = N(g_{eff}\,\mu_B)^2 S(S+1)/3k_B\rho$. Here, N is the number of cations per unit volume, g_{eff} is the effective gyromagnetic factor of Mn ion, S is the spin, ρ is the mass density calculated from the lattice parameters, and μ_B denotes the Bohr magneton. Here, we assume that $S = 5/2$ and $g_{eff} = 2$.

The results of the fitting procedure are given in Table 2. For all of the samples, the negative values of the Curie–Weiss temperature θ were determined, which indicates that antiferromagnetic (AF) interactions are predominant in the measured samples. The negative values of the Curie–Weiss temperature have already been reported for ZrO_2:Mn [14,23–25]. In our paper, we focus on the influence of the synthesis procedure on the resultant magnetic properties, e.g., the Curie–Weiss temperature. The inspection of Table 2 shows that the obtained values of the Curie–Weiss temperature strongly depend on the conditions of the preparation procedure. Lower values of θ were obtained for samples prepared by the use of $MnCl_2$ and $Mn(NO_3)_2$ precursors. Three samples doped with 4.9 wt % of Mn (P5, P9, P12) were prepared with the same pH value (pH = 9) and by the use of three different precursors. We determined that $\theta = -2.5$ K for the $KMnO_4$ precursor, $\theta = -1.8$ K for the $MnCl_2$ precursor, and $\theta = -1$ K for the $Mn(NO_3)_2$ precursor. The same tendency was observed for samples doped with a higher Mn content. For two samples doped with 9.8 wt % of Mn and prepared with pH = 9, we determined that $\theta = -5.7$ K for the $MnCl_2$ precursor and $\theta = -4.7$ K for the $Mn(NO_3)_2$ precursor. For the $KMnO_4$ precursor, we studied the influence of the pH of the reaction mixture used for the synthesis. Figure 4 shows the dependence of the Curie–Weiss temperature θ on the pH value. We observed a distinct increase in the absolute values of the Curie–Weiss temperature θ with the

increase of pH values. It suggests that the antiferromagnetic interactions are strengthened with an increase of the pH value. The Curie–Weiss temperature can be tuned by the appropriate selection of the synthesis conditions. For example, in the case of the $KMnO_4$ precursor and pH = 9, for 19.5 wt % of Mn, the absolute values of θ can be much decreased: from −17.4 K to −6.1 K by the decrease of the pH value from pH = 9 to pH = 3.

We calculated the concentration of Mn ions from the determined C parameter using Equation (1). The obtained values are lower than those of the nominal content. The observed discrepancy can be related to the efficiency of the used synthesis process. The calculated values of x depend on the used pH values. The higher concentration values are obtained for lower values of pH. The Curie–Weiss temperature $\theta(x)$ depends on the content of Mn ions. Using the theory of Spałek et al. [32], one can express $\theta(x)$ as: $\theta(x) = \theta_0 x$. The analysis of the results gathered in Table 2 shows that the observed large changes of θ values with pH values (for the same nominal content of Mn) are not related to the changes of the content of Mn ions. The results suggest that an increase in pH values enhances the strength of antiferromagnetic interactions.

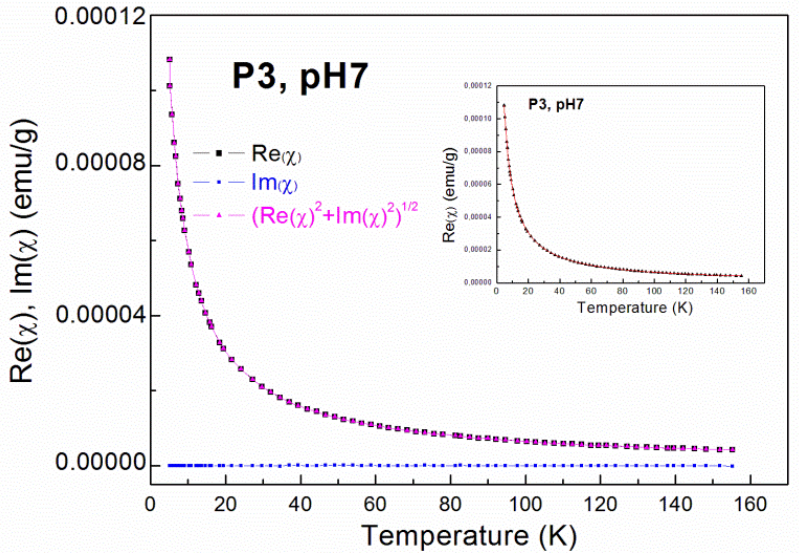

(**a**)

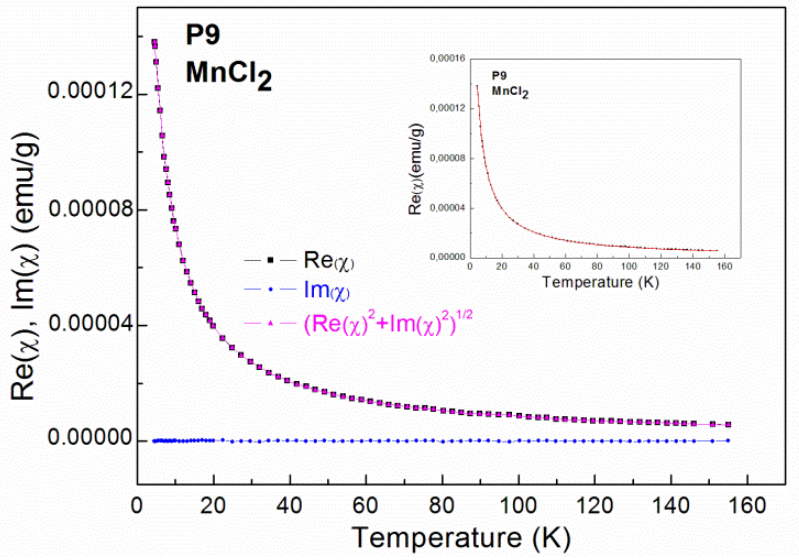

(**b**)

Figure 3. *Cont.*

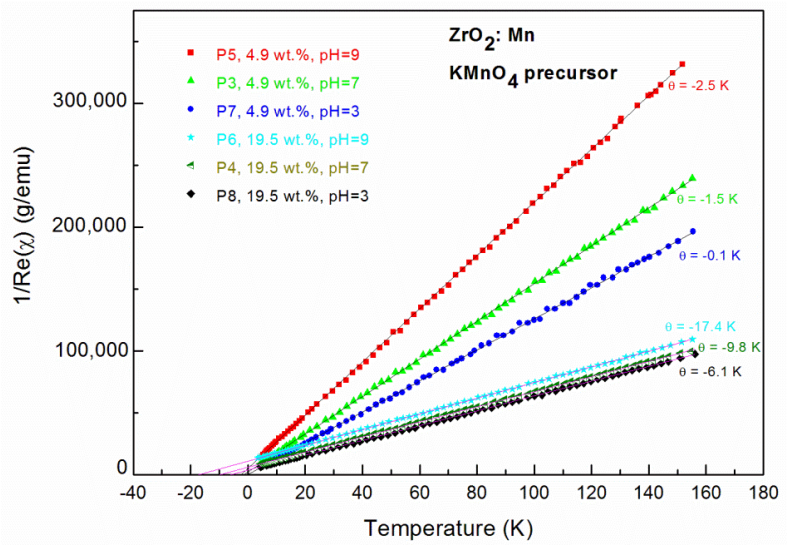

(**c**)

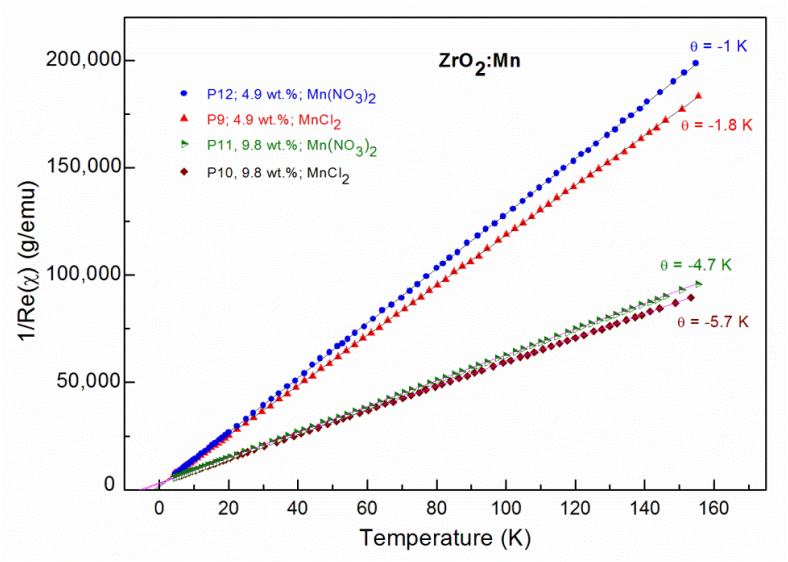

(**d**)

Figure 3. Alternating current (AC) magnetic susceptibility data; The real part ($Re(\chi)$) and imaginary ($Im(\chi)$) part of AC magnetic susceptibility as well as the calculated $\chi = (Re(\chi)^2 + Im(\chi)^2)^{1/2}$ for: (**a**) the P3 sample; (**b**) the P4 sample, where the insets show fitting curves (red solid lines); The inverse magnetic susceptibility for nanocrystalline ZrO_2:Mn samples synthesized with: (**c**) the $KMnO_4$ precursor; (**d**) the $MnCl_2$ and $Mn(NO_3)_2$ precursors.

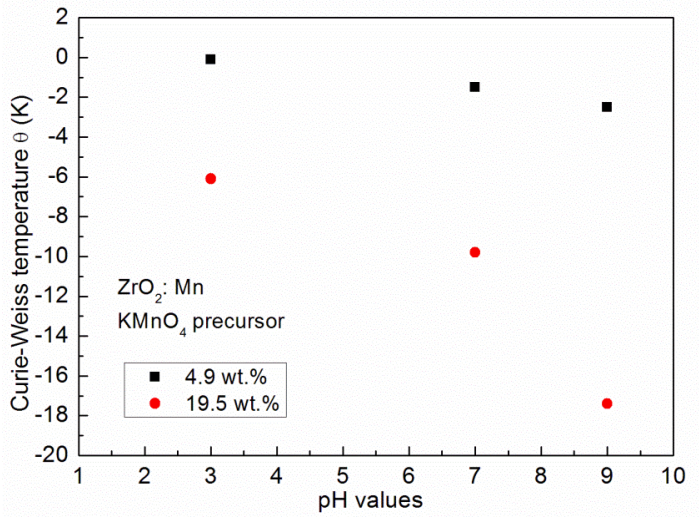

Figure 4. The Curie–Weiss temperature dependence on the pH value of the reaction mixture used in the synthesis.

Table 2. The values of parameters C and θ determined from fits to the Curie–Weiss law for ZrO_2:Mn. The parameter x was determined from: $C(x) = C_0x$, $C_0 = N(g_{eff}\,\mu_B)^2S(S+1)/3k_B\rho$. The values of the parameters x_{eff} and T_{eff} were determined from fits to the effective Brillouin function law for ZrO_2:Mn.

Sample	θ (K)	C (emuK/g)	x	x_{eff}	T_{eff} (K)
P7 4.9 wt % pH 3; $KMnO_4$	−0.1	0.00080	0.022 (0.99 wt %)	0.018 (0.81 wt %)	1.48
P3 4.9 wt % pH 7; $KMnO_4$	−1.5	0.00066	0.018 (0.80 wt %)	0.015 (0.67 wt %)	1.77
P5 4.9 wt % pH 9; $KMnO_4$	−2.5	0.00470	0.013 (0.58 wt %)	0.010 (0.45 wt %)	1.36
P8 19.5 wt % pH 3; $KMnO_4$	−6.1	0.00167	0.046 (2.08 wt %)	0.032 (1.44 wt %)	3.13
P4 19.5 wt % pH 7; $KMnO_4$	−9.8	0.00164	0.045 (2.01 wt %)	0.024 (1.08 wt %)	3.71
P6 19.5 wt % pH 9; $KMnO_4$	−17.4	0.00158	0.044 (2.00 wt %)	0.018 (0.81 wt %)	3.21
P9 4.9 wt % pH 9; $MnCl_2$	−1.8	0.00086	0.024 (1.08 wt %)	0.021 (0.94 wt %)	2.56
P12 4.9 wt % pH 9; $Mn(NO_3)_2$	−1	0.00079	0.022 (0.99 wt %)	0.021 (0.94 wt %)	2.29
P10 9.8 wt % pH 9; $MnCl_2$	−5.7	0.00178	0.049 (2.20 wt %)	0.031 (1.40 wt %)	2.58
P11 9.8 wt % pH 9; $Mn(NO_3)_2$	−4.7	0.00167	0.046 (2.08 wt %)	0.031 (1.40 wt %)	2.87

Magnetization (M) up to 50 K as a function of magnetic field (B) up to 9 T is shown in Figure 5a–c. The magnetic measurements revealed no hysteresis and no saturation. No evidence of ferromagnetism was observed.

The data do not fit well to the standard Brillouin function (not shown) possibly because of the presence of antiferromagnetic (AF) interactions between magnetic ions. Taking into account the weak

saturation effect due to the AF interactions between Mn ions, a reasonable fit was obtained by using the phenomenological equation [33]:

$$M(B,T) = S\, g\, \mu_B\, N\, x_{eff}\, B_S(B,T_{eff}), \quad (2)$$

where B_S is the Brillouin function for a spin $S = 5/2$, $T_{eff} = T + T_0$ and x_{eff} are the fitting parameters, N is the number of cations per unit mass, $g = 2$ is the Landé factor, and μ_B is the Bohr magneton.

The so-called effective Brillouin function, $B_s(B,T_{eff})$, has been widely and successfully used to describe the magnetization of diluted magnetic semiconductors. It is worth noting that the value of the x_{eff} parameter represents an effective molar fraction of active Mn and is usually smaller than the real concentration of magnetic ions due to antiferromagnetic interactions between magnetic ions [33]. The value of $T_0 < T$ is a signature of an AF coupling between Mn ions [33]. The solid curves (Figure 5a–c) are the fitting results of experimental data at 4.5 K. The fitting values are shown in Table 2. It is clearly visible that fitting values of x_{eff} decrease with the increase of pH values. For example, in the case of samples doped with 4.9 wt % by the use of $KMnO_4$ precursor, we obtained: $x_{eff} = 0.018$ (0.81 wt %) for pH = 3 (the P7 sample), $x_{eff} = 0.015$ (0.67 wt %) for pH = 7 (the P3 sample), and $x_{eff} = 0.010$ (0.45 wt %) for pH = 9 (the P5 sample). The same tendency is visible for samples doped with a higher Mn concentration (19.5 wt %). We obtained: $x_{eff} = 0.032$ (1.44 wt %) for pH = 3 (the P8 sample), $x_{eff} = 0.024$ (1.08 wt %) for pH = 7 (the P4 sample), and $x_{eff} = 0.018$ (0.81 wt %) for pH = 9 (the P6 sample). It means that an increase in pH values leads to a decrease in the Mn content in the ZrO_2 structure. A large discrepancy between the nominal content and the x_{eff} parameter was also observed by J. Yu et al. [23]. The authors [23], similarly to our results, observed that the ratio of the x_{eff} parameter to the nominal content decreased with the increase of x and suggested the enhancement of antiferromagnetic interactions between the doped magnetic ions. For our samples, a similar effect was also observed. The obtained values of x_{eff} are lower than the values of x calculated from the AC susceptibility fitting parameter $C(x)$. However, we recall that lower values of x_{eff} reflect the antiferromagnetic interactions between Mn ions.

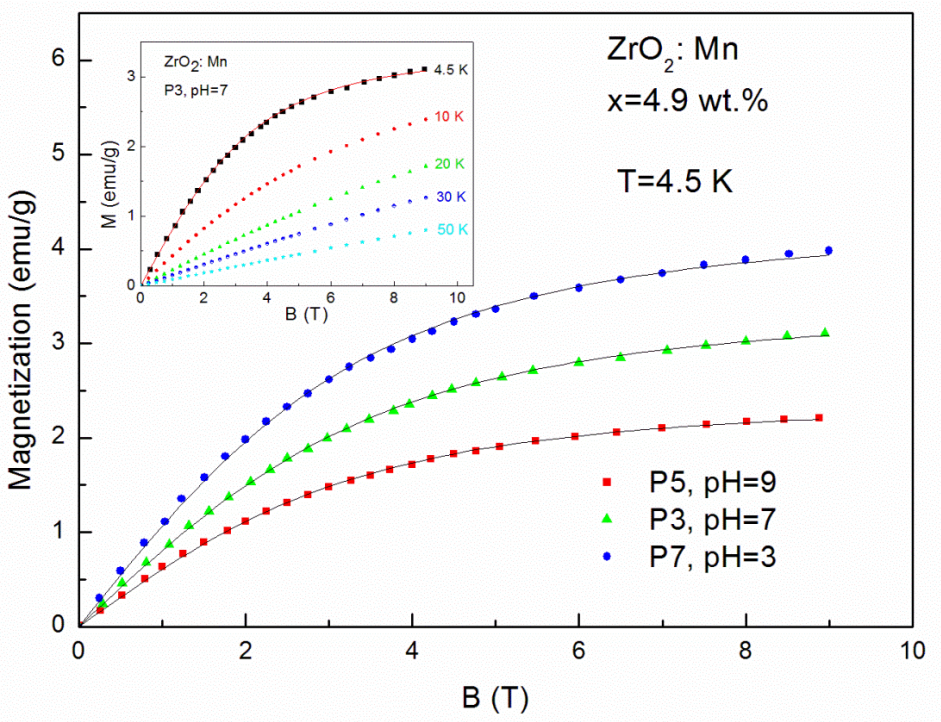

(**a**)

Figure 5. *Cont.*

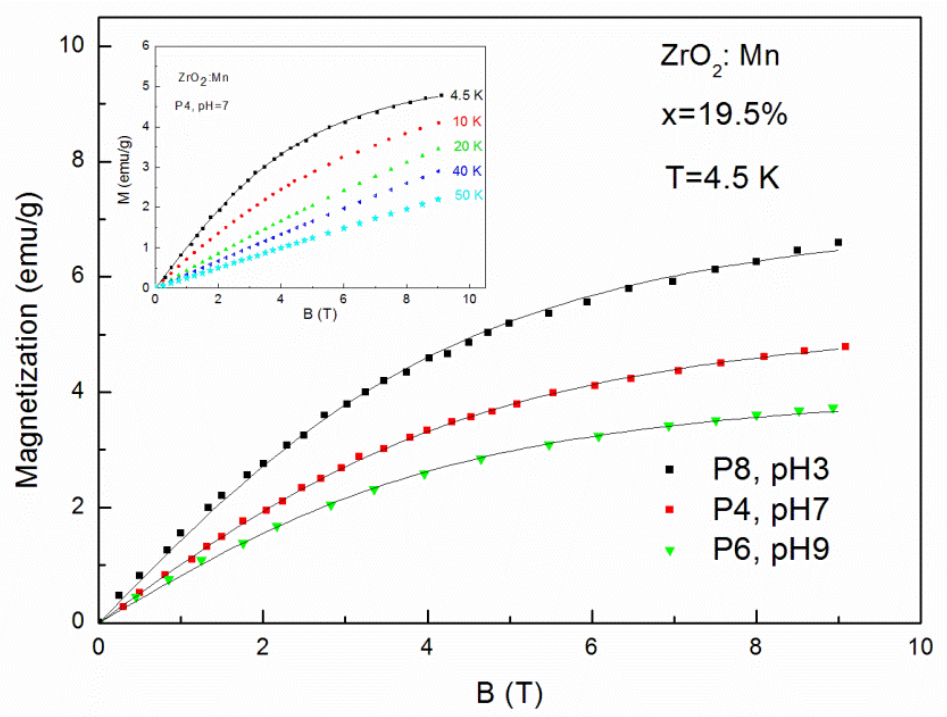

(**b**)

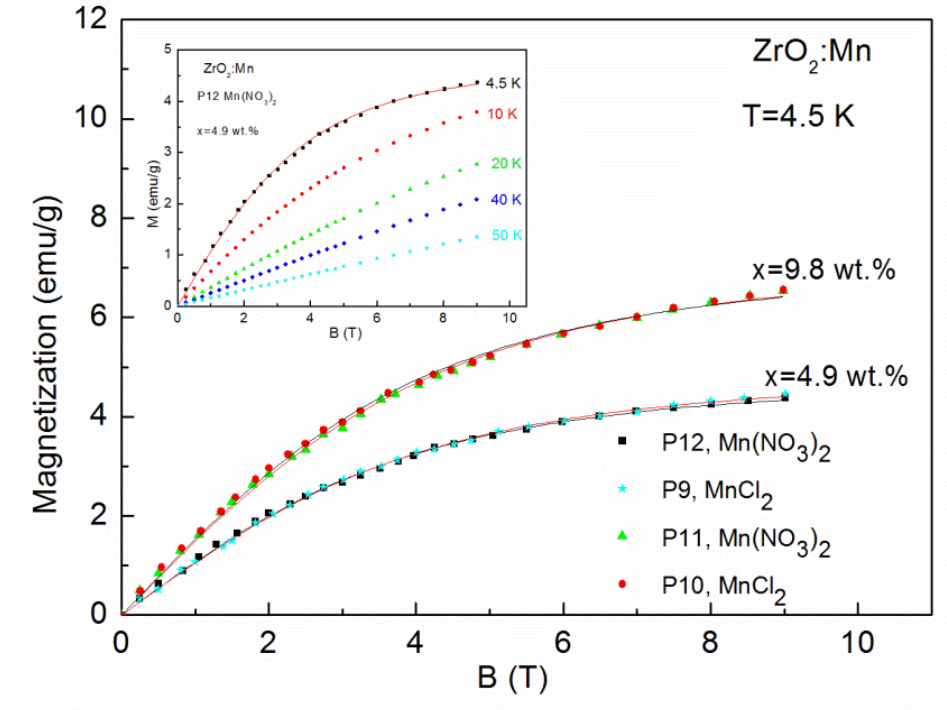

(**c**)

Figure 5. The magnetization data measured up to 9 T for: (**a**) ZrO_2 doped with 4.9 wt % of Mn samples prepared by use of $KMnO_4$ precursor with different pH values (pH = 3, pH = 7, pH = 9) at T = 4.5 K and sample P3 for selected temperatures (inset); (**b**) ZrO_2 samples doped with 19.5 wt % of Mn prepared by use of $KMnO_4$ precursor with different pH values (pH = 3, pH = 7, pH = 9) at T = 4.5 K and sample P4 for selected temperatures (inset); (**c**) samples doped with 4.9 wt % of Mn and 9.8 wt % of Mn prepared with $MnCl_2$ and $Mn(NO_3)_2$ precursors at T = 4.5 K and sample P12 and doped with 4.9 wt % of Mn for selected temperatures (inset).

4. Conclusions

We have studied the structural and magnetic properties of nanocrystalline ZrO_2 doped with Mn in hydrothermal synthesis. We have shown that the formation of high-temperature crystal phases strongly depends on the synthesis conditions, e.g., the type of the precursor. We examined three types of precursors: $KMnO_4$, $MnCl_2$, and $Mn(NO_3)_2$. Using these two last precursors ($MnCl_2$ and $Mn(NO_3)_2$) leads to the formation of pure cubic ZrO_2 phase (for nominal 9.8 wt % of Mn). Our experimental results suggest that using $KMnO_4$ precursor does not lead to the formation of cubic phase of ZrO_2. In that case, we noticed that an increase of pH values decreases the amount of monoclinic phase and increases the amount of tetragonal phase. We showed that changing the pH value allows for adjusting the magnetic parameters. In particular, it is possible to obtain a material with a desired Curie–Weiss temperature. Thus, the strength of antiferromagnetic interactions can be suppressed by adjusting the chemical synthesis conditions.

Author Contributions: Conceptualization, I.K.-K. and W.D.; Magnetic investigations, I.K.-K. and M.A.; Data analysis, I.K.-K. and R.M.; Synthesis and STEM measurements, A.M. and L.S.; XRD investigations, R.M.; Manuscript writing, I.K.-K.

Conflicts of Interest: The authors declare no conflict of interest.

References

1. Yadav, G.D.; Nair, J.J. Sulfated zirconia and its modified versions as promising catalysts for industrial processes. *Microporous Mesoporous Mater.* **1999**, *33*, 1–48. [CrossRef]
2. Lee, D.S.; Kim, W.S.; Choi, S.H.; Kim, J.; Lee, H.W.; Lee, J.H. Characterization of ZrO_2 codoped with Sc_2O_3 and CeO_2 electrolyte for the application of intermediate temperature SOFCs. *Solid State Ion.* **2005**, *176*, 33–39. [CrossRef]
3. Badwal, S.P.S. Stability of Solid Oxide Fuel Cell Components. *Solid State Ion.* **2001**, *143*, 39–46. [CrossRef]
4. Minh, N.Q. Ceramic Fuel Cells. *J. Am. Ceram. Soc.* **1993**, *76*, 563–588. [CrossRef]
5. French, R.H.; Glass, S.J.; Ohuchi, F.S.; Xu, Y.N.; Ching, W.Y. Experimental and theoretical determination of the electronic structure and optical properties of three phases of ZrO_2. *Phys. Rev. B* **1994**, *49*, 5133–5142. [CrossRef]
6. Yashima, M.; Hirose, T.; Katano, S.; Suzuki, Y.; Kakihana, M.; Yoshimura, M. Structural changes of ZrO_2-CeO_2 solid solutions around the monoclinic-tetragonal phase boundary. *Phys. Rev. B* **1995**, *51*, 8018–8025. [CrossRef]
7. Albanese, E.; Leccese, M.; Di Valentin, C.; Pacchioni, G. Magnetic properties of nitrogen doped ZrO_2: Theoretical evidence of absence of room temperature ferromagnetism. *Sci. Rep.* **2016**, *6*, 31435–31445. [CrossRef] [PubMed]
8. Bacquet, G.; Dugas, J.; Escribe, C.; Rouanet, A. The system ZrO_2 CaO studied by the electron spin resonance of Mn^{2+} ions. *J. Solid State Chem.* **1976**, *19*, 251–261. [CrossRef]
9. Appel, C.C.; Bonanos, N.; Horsewell, A.; Linderoth, S. Ageing behaviour of zirconia stabilised by yttria and manganese oxide. *J. Mater. Sci.* **2001**, *36*, 4493–4501. [CrossRef]
10. Hannink, R.H.J. Microstructural development of sub-eutectoid aged MgO-ZrO_2 alloys. *J. Mater. Sci.* **1983**, *18*, 457–470. [CrossRef]
11. Zippel, J.; Lorenz, M.; Lenzner, J.; Grundmann, M.; Hammer, T.; Jacquot, A.; Böttner, H. Electrical transport and optical emission of $Mn_xZr_{1-x}O_2$ ($0 \leq x \leq 0.5$) $Mn_xZr_{1-x}O_2$ ($0 \leq x \leq 0.5$) thin films. *J. Appl. Phys.* **2001**, *110*, 043706. [CrossRef]
12. Dimri, M.C.; Kooskora, H.; Pahapill, J.; Joon, E.; Heinmaa, I.; Subbi, J.; Stern, R. Search for ferromagnetism in manganese-stabilized zirconia. *Phys. Status Solidi A* **2011**, *208*, 172–179. [CrossRef]
13. Saravanakumra, S.; Kamalaveni, J.; Rani, M.P.; Saravanan, R. Solubility of Mn stabilized cubic zirconia nanostructures. *J. Mater. Sci. Mater. Electron.* **2014**, *25*, 837–843. [CrossRef]
14. Pucci, A.; Clavel, G.; Willinger, M.-G.; Zitoun, D.; Pinna, N. Transition metal-doped ZrO_2 and HfO_2 nanocrystals. *J. Phys. Chem. C* **2009**, *113*, 12048–12052. [CrossRef]
15. Pearton, S.J.; Heo, W.H.; Ivill, M.; Norton, D.P.; Steiner, T. Dilute magnetic semiconducting oxides. *Semicond. Sci. Technol.* **2004**, *19*, R59–R74. [CrossRef]

16. Kuryliszyn-Kudelska, I.; Hadžić, B.; Sibera, D.; Romčević, M.; Romčević, N.; Narkiewicz, U.; Dobrowolski, W. Dynamic magnetic properties of ZnO nanocrystals incorporating Fe. *J. Alloys Compd.* **2011**, *509*, 3756–3759. [CrossRef]
17. Kuryliszyn-Kudelska, I.; Dobrowolski, W.; Arciszewska, M.; Romčević, N.; Romčević, M.; Hadžić, B.; Sibera, D.; Narkiewicz, U.; Łojkowski, W. Transition metals in ZnO nanocrystals—Magnetic and structural properties. *Sci. Sinter.* **2013**, *45*, 31–48. [CrossRef]
18. Hong, N.H.; Kanoun, M.B.; Goumri-Said, S.; Song, J.-H.; Chikoidze, E.; Dumont, Y.; Ruyter, A.; Kurisu, M. The origin of magnetism in transition metal-doped ZrO_2 thin films: Experiment and theory. *J. Phys. Condens. Matter* **2013**, *25*, 436003–436010. [CrossRef] [PubMed]
19. Sundaresan, A.; Bhagavi, R.; Rangarajan, N.; Siddesh, U.; Rao, C.N.R. Ferromagnetism as a universal feature of nanoparticles of the otherwise nonmagnetic oxides. *Phys. Rev. B* **2006**, *74*, 161306(R). [CrossRef]
20. Venkatesan, M.; Fitzgerald, C.B.; Coey, J.M.D. Thin films: Unexpected magnetism in a dielectric oxide. *Nature* **2004**, *430*, 630. [CrossRef] [PubMed]
21. Ostanin, S.; Ernst, A.; Sandratskii, L.M.; Bruno, P.; Dane, M.; Dughes, I.D.; Staunton, J.B.; Hergert, W.; Mertig, I.; Kudrnovsky, J. Mn-stabilized zirconia: From imitation diamonds to a new potential high-T_C ferromagnetic spintronics material. *Phys. Rev. Lett.* **2007**, *98*, 016101. [CrossRef] [PubMed]
22. Boujnah, M.; Zaari, H.; Benyoussef, A.; El Kenz, A.; Mounkachi, O. Understanding ferromagnetism and optical absorption in 3D transition metal-doped cubic ZrO_2 with the modified Becke-Johnson exchange-correlation functional. *J. Appl. Phys.* **2014**, *115*, 123909–123916. [CrossRef]
23. Yu, J.; Duan, L.B.; Yang, Y.C.; Rao, G.H. Absence of ferromagnetism in Mn- and Fe-stabilized zirconia nanoparticles. *Physica B* **2008**, *403*, 4264–4268. [CrossRef]
24. Clavel, G.; Willinger, M.G.; Zioun, D.; Pinna, N. Manganese-doped zirconia nanocrystals. *Eur. J. Inorg. Chem.* **2008**, *6*, 863–868. [CrossRef]
25. Srivastava, S.K.; Lejay, P.; Barbara, B.; Boisron, O.; Pailhes, S.; Bouzerar, G. Absence of ferromagnetism in Mn-doped tetragonal zirconia. *J. Appl. Phys.* **2011**, *110*, 043929. [CrossRef]
26. Zippel, J.; Lorenz, M.; Setzer, A.; Wagner, G.; Sobolev, N.; Esquinazi, P.; Grundmann, M. Defect-induced ferromagnetism in undoped and Mn-doped zirconia thin films. *Phys. Rev. B* **2010**, *82*, 125209–125214. [CrossRef]
27. Hong, N.H.; Park, C.K.; Raghavender, A.T.; Ciftja, O.; Bingham, N.S.; Phan, M.H.; Srikanth, H. Room ferromagnetism in monoclinic Mn-doped ZrO_2 thin films. *J. Appl. Phys.* **2012**, *111*, 07C302. [CrossRef]
28. Kumar, S.; Ojha, A.K. Room temperature ferromagnetism in undoped and Mn doped t-ZrO_2 nanostructures originated due to oxygen vacancy and effect of Mn doping on its optical properties. *Mater. Chem. Phys.* **2016**, *169*, 13–20. [CrossRef]
29. Kuryliszyn-Kudelska, I.; Arciszewska, M.; Małolepszy, A.; Mazurkiewicz, M.; Stobiński, L.; Grabias, A.; Kopcewicz, M.; Paszkowicz, W.; Minikaev, R.; Domukhovski, V.; et al. Influence of Fe doping on magnetic properties of ZrO_2 nanocrystals. *J. Alloys Compd.* **2015**, *632*, 609–615. [CrossRef]
30. Patterson, A.L. The Scherrer Formula for X-ray Particle Size Determination. *Phys. Rev.* **1939**, *56*, 978–982. [CrossRef]
31. Buschow, K.H.J.; de Boer, F.R. *Physics of Magnetism and Magnetic Materials*; Plenum Publishers: New York, NY, USA, 2003; ISBN 978-0-306-48408-7.
32. Spałek, J.; Lewicki, A.; Tarnawski, Z.; Furdyna, J.K.; Gałązka, R.R.; Obuszko, Z. Magnetic susceptibility of semiconductors: High-temperature regime and the role of superexchang. *Phys. Rev. B* **1986**, *33*, 3407–3418. [CrossRef]
33. Gaj, J.A.; Planel, R.; Fishman, G. Relation of magneto-optical properties of free excitonic to spin alignment of Mn^{2+} ions in $Cd_{1-x}Mn_xTe$. *Solid State Commun.* **1979**, *29*, 435–438. [CrossRef]